

Modelling multi-wavelength observational characteristics of bow shocks from runaway early type stars

David M. Acreman^{1*}, Ian R. Stevens² and Tim J. Harries¹

¹ *School of Physics and Astronomy, University of Exeter, Stocker Road, Exeter EX4 4QL.*

² *School of Physics and Astronomy, University of Birmingham, Edgbaston, Birmingham, B15 2TT, UK*

11 October 2018

ABSTRACT

We assess the multi-wavelength observable properties of the bow shock around a runaway early type star using a combination of hydrodynamical modelling, radiative transfer calculations and synthetic imaging. Instabilities associated with the forward shock produce dense knots of material which are warm, ionised and contain dust. These knots of material are responsible for the majority of emission at far infra-red, $H\alpha$ and radio wavelengths. The large scale bow shock morphology is very similar and differences are primarily due to variations in the assumed spatial resolution. However infra-red intensity slices (at 22 microns and 12 microns) show that the effects of a temperature gradient can be resolved at a realistic spatial resolution for an object at a distance of 1 kpc.

Key words: stars: early-type - ISM: general

1 INTRODUCTION

Stars with large velocities ($> 40 \text{ km s}^{-1}$) relative to the surrounding interstellar medium (ISM) are termed runaway stars (Blaauw 1961; Cruz-González et al. 1974; Tetzlaff et al. 2011). Space velocities up to 200 km s^{-1} were observed by Blaauw (1961) and if conditions in the ISM are favourable the velocity of a runaway star relative to the ISM will be supersonic (Huthoff & Kaper 2002) leading to the formation of a bow shock (Baranov et al. 1976). Runaway early-type stars have strong stellar winds and experience a particularly strong interaction with the ISM, due to the high space velocity of the star and the high velocity of the wind. A number of high velocity early-type stars were identified by Blaauw (1961) and Cruz-González et al. (1974). Bow shocks have also been seen around evolved stars, e.g. red super-giants (Noriega-Crespo et al. 1997a; Cox et al. 2012; Gvaramadze et al. 2014; Meyer et al. 2014a). These bow shocks are similar to those around early-type, main sequence stars albeit with a lower stellar wind velocity.

It has been proposed that runaway stars are produced by binary supernovae (Blaauw 1961) or result from dynamical interactions between stars in a cluster (Poveda et al. 1967). There is evidence that, in practice, runaway stars are produced by both mechanisms (Portegies Zwart 2000; Hoogerwerf et al. 2000, 2001). Runaway stars with velocities of a few 100 km s^{-1} can be generated by both the bi-

nary supernova (Portegies Zwart 2000) and dynamical ejection scenarios (Poveda et al. 1967; Leonard 1991). Moreover, ejection from the Galactic centre, due to interaction with the supermassive black hole, has been cited as a mechanism for the formation of hypervelocity stars with even higher spatial velocities (Hills 1988; Brown et al. 2012). In addition to bow shocks around stars with large peculiar velocities, young stars in a cluster can drive outflows, which cause ISM velocities to deviate from the local standard of rest, and bow shocks can be generated without ejecting stars from the cluster (Povich et al. 2008).

The formation of isolated massive stars is an important factor in discriminating between different star formation mechanisms. In the competitive accretion paradigm massive stars form by accreting material in a cluster environment (Zinnecker 1982; Larson 1992; Bonnell et al. 1997, 2004) whereas in the core accretion paradigm massive stars are able to form in isolation (Wolfire & Cassinelli 1987; Yorke & Sonnhalter 2002; Krumholz et al. 2009). When searching for evidence of isolated massive star formation runaways need to be excluded, as they are likely to be found far from where they formed (de Wit et al. 2005; Bressert et al. 2012). Runaway stars can sometimes be identified through proper motion observations or line-of-sight velocity measurements but the presence of a bow shock is also a valuable indication that a star is a runaway. Stellar bow shocks yield not only kinematic information but the stand-off distance of the shock has been used as a diagnostic of stellar wind and ISM properties (Brown & Bomans 2005; Povich et al. 2008; Kobulnicky

* E-mail acreman@astro.ex.ac.uk

et al. 2010; Cox et al. 2012). As well as using bow shocks as diagnostics it is important to understand the observable properties of stellar bow shocks, as they may produce an infra-red excess which could be confused with emission from a circumstellar disc (Povich et al. 2008; Gáspár et al. 2008).

Observational studies have detected stellar bow shocks in various regions of the spectrum, most notably in the mid-infrared (Noriega-Crespo et al. 1997b; van Buren & McCray 1988; Gáspár et al. 2008; Povich et al. 2008; Kobulnicky et al. 2010; Peri et al. 2012) but also in other regimes e.g. H α observations by Brown & Bomans (2005). A multi-wavelength study of the O5 star HD 192281 by Arnal et al. (2011) revealed an H I structure consistent with formation by a bow shock, with counterparts seen in infrared, radio continuum and CO (1–0) observations. The radio emission had a thermal spectrum with ionisation as the proposed source. Non-thermal radio emission, from relativistic particles, has been detected in observations of BD+43°3654 by Benaglia et al. (2010) and non-thermal X-ray emission from the AE Aur bow shock was detected by López-Santiago et al. (2012).

Analytical expressions can be derived for some bow shock properties, given certain simplifying assumptions. Wilkin (1996) treats the bow shock as an axisymmetric thin shell and calculates analytical expressions for the shape, mass column density and velocity of the shocked gas. However when the simplifying assumptions are relaxed numerical modelling is required. In their study of ultracompact H II regions Mac Low et al. (1991) use a numerical model of a shell in momentum balance. This gives a two-dimensional solution which they use to produce synthetic radio observations. Raga et al. (1997) use two-dimensional models, with hydrodynamics and a radiative transfer approximation, to produce synthetic dust and H α emission maps for a runaway O star. A number of subsequent studies have also made use of two-dimensional hydrodynamics to study the physics of bow shocks around runaway massive stars e.g. Comeron & Kaper (1998); Cox et al. (2012). More recently (Meyer et al. 2014b) modelled an evolving main sequence star, using a two-dimensional hydrodynamics code, and generated synthetic H α observations.

In this paper we model the bow shock caused by a runaway early type star and determine the observational properties of the resulting structure. To achieve this we combine hydrodynamical modelling (described in Section 2) with Monte-Carlo radiative transfer calculations (described in Section 3) to model the radiation influenced region around the star. We generate synthetic observables, as described in Section 4, focussing on the infra-red, H α and radio regimes where successful detections of stellar bow shocks have already been made. We discuss our results in Section 5, where we compare them to synthetic observations in the literature, and discuss assumptions and potential improvements to the model. We close with our conclusions in Section 6.

2 HYDRODYNAMIC CALCULATION

The formation of the bow shock structure was modelled using the VH-1 hydrodynamics code (Blondin et al. 2003; Hawley et al. 2012), a grid-based code which uses the Piecewise-Parabolic Method (Colella & Woodward 1984) and provides good resolution of shocks in complex flows. The gas is

Table 1. Parameters of the hydrodynamical simulation

Parameter		Value
Stellar mass-loss rate	\dot{M}_W	$10^{-5} M_{\odot} \text{yr}^{-1}$
Stellar wind velocity	V_W	2000 km s^{-1}
Stellar velocity	V_*	100 km s^{-1}
ISM number density	n_{ISM}	1000 cm^{-3}
Grid size		10^{18} cm
Number of grid cells		1000^2

treated as an ideal gas with radiative cooling implemented as a cooling curve. The radiative cooling in the hydrodynamic calculation is modelled using an analytic fit to the results of Schure et al. (2009), assuming a solar metallicity plasma. Radiation pressure is not included and no additional physical viscosity is added.

The simulation grid uses two dimensional, cylindrical polar co-ordinates, with the direction of motion of the star aligned with the z-axis. The grid size is 10^{18} cm in each linear dimension with 1000 grid cells. The star is placed on the z-axis and ISM material flows onto the grid at a fixed velocity of 100 km s^{-1} (i.e. the simulation is performed in the frame of reference of the star). The star has a wind which causes material to flow radially outwards and meet the incoming ISM in the upstream direction. The stellar wind is implemented as a region with a constant outflow velocity which is imposed within a fixed radius of 50 grid cells from the star. The density in the outflow region decreases with radius such that the mass loss rate is constant. The wind radius must be large enough to ensure that the wind remains spherical but needs to be smaller than the minimum extent of the bow shock region. The main model parameters are listed in Table 1. Dust mass is not included in the hydrodynamical simulations, where its contribution to the mass is negligible. However radiation pressure can have a significant impact on dust dynamics which could influence the gas if the dust and gas are dynamically coupled (Villaver et al. 2012; Ochsendorf et al. 2014; Gratier et al. 2014). Dust opacity is included in the radiative transfer calculation, where the effect is significant (see Section 3).

The density distribution is plotted in Fig. 1 (top left) and shows a two shock structure with a forward shock, where the ISM shocks, and an inner shock where the stellar wind terminates. This is similar to the structures seen in other simulations (e.g. Comeron & Kaper 1998; Cox et al. 2012; Mackey et al. 2012; Meyer et al. 2014b) where the two shocks bound a contact discontinuity. However our model does not show a clear separation between the forward shock and contact discontinuity. If the shocked ambient gas cools very rapidly, as expected due to the high ISM density, then the outer layer of hot material is not present, as described by Comeron & Kaper (1998). The forward shock is subject to instabilities which result in the formation of denser knots of material. Similar instabilities have been seen in other numerical models of stellar bow shocks (e.g. Comeron & Kaper (1998), Cox et al. (2012) and Meyer et al. (2014b)). A number of different mechanisms can generate these instabilities (e.g. Kelvin-Helmholtz instabilities, non-linear thin shell instabilities (Vishniac 1994) and transverse acceleration instabilities (Dgani et al. 1996)) as discussed by Comeron & Kaper (1998).

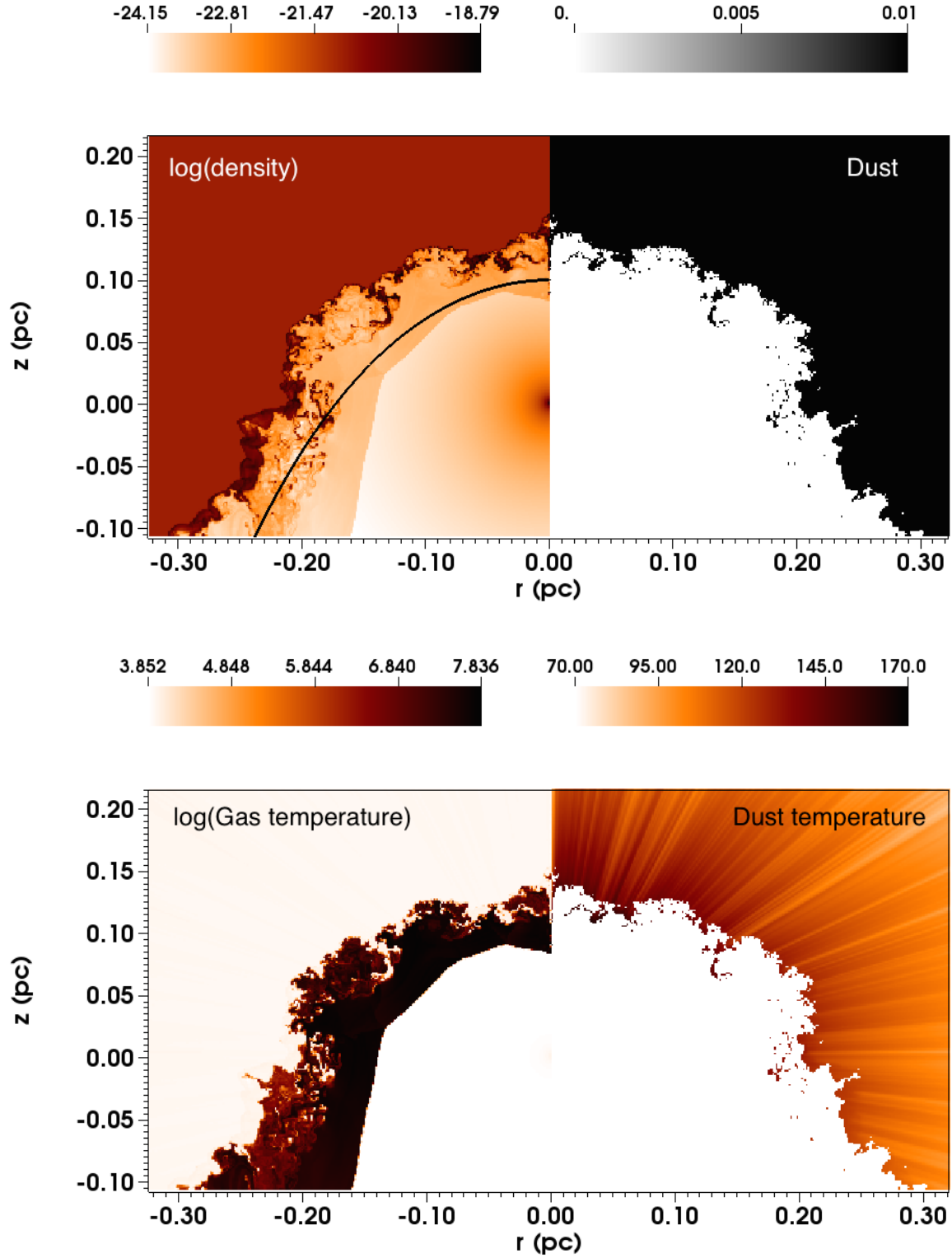


Figure 1. Density (top left) in gm cm^{-3} , dust distribution (top right), gas temperature (bottom left) in K, and dust temperature (bottom right) in K, at the end of the photoionisation equilibrium calculation. The star is located at the origin of the grid. The black curve shown on the density plot is the Wilkin analytical solution. The dust distribution plot shows dust fraction by mass and is black where dust is present and white where there is no dust.

An analytical expression for the shock stand-off distance R_0 can be derived by determining the distance at which the stellar wind ram pressure and the ISM ram pressure are equal (Wilkin 1996)

$$R_0 = \sqrt{\frac{\dot{M}_W V_W}{4\pi \rho_{\text{ISM}} V_*^2}} \quad (1)$$

where ρ_{ISM} is the ISM mass density and other symbols are defined in Table 1. We assume the ISM is composed of hydrogen and helium with a 10:1 ratio and is fully ionised. The ISM number density n_{ISM} is the sum of the hydrogen ion, helium ion and electron number densities (i.e. $n_{\text{ISM}} = n_{\text{H}^+} + n_{\text{He}^{++}} + n_{e^-}$) and $\rho_{\text{ISM}} = \frac{14}{23} n_{\text{ISM}} m_H$ where m_H is the mass of a hydrogen atom. For the parameters used in this simulation the calculated stand-off distance is $R_0 = 0.10$ pc. Wilkin (1996) derives an analytical expression for the shape of the bow shock

$$R = R_0 \csc \theta \sqrt{3(1 - \theta \cot \theta)} \quad (2)$$

where R is the distance from the star and θ is the polar angle from the axis of symmetry. The analytical solution is shown in Fig. 1 as a black curve overlaid on the density plot. In our model the z-axis location of the stand-off distance is between the forward shock and the wind termination (inner) shock. The shape of the forward shock follows the analytical solution but is located further from the star. The post-stellar wind material in our model is at a high temperature and the density ratio is approximately 4 which suggest an adiabatic shock with inefficient cooling of the shocked gas. Comeron & Kaper (1998) note that if cooling of the shocked stellar wind is inefficient then a layer of hot, low density gas lies between the stellar wind and the bow shock, causing the bow shock to move forward of R_0 .

3 PHOTOIONISATION CALCULATION

The density distribution from the hydrodynamical calculation, described in Section 2, is used as input to the TORUS¹ radiative transfer code (Harries 2000). The VH-1 density field is mapped onto a TORUS grid comprising 256×256 cells². This density field is used to calculate temperature and ionisation equilibrium using an iterative Monte-Carlo method, similar to that of Ercolano et al. (2003) and Wood et al. (2004). The photoionisation component of TORUS has been described in detail by Haworth & Harries (2012) and Haworth et al. (2015). For the calculations presented in this paper the photoionisation calculation operates stand-alone (without a TORUS hydrodynamics calculation) using a static density distribution derived from the VH-1 calculation. Consequently we are able to use a more computationally expensive determination of equilibrium temperature (based on the balance between ionisation, recombination and forbidden line cooling) rather than the simplified thermal balance calculation of Haworth & Harries (2012). Like Haworth & Harries (2012) we use a polychromatic radiation field and explicitly represent the diffuse radiation field (i.e. there is

Table 2. Elements and species included in the photoionisation calculation with elemental abundances relative to hydrogen.

Element	Species	Abundance
H	I,II	1
He	I,II,III	0.1
C	I,II,III,IV	2.2×10^{-4}
N	I,II,III	4×10^{-5}
O	I,II,III	3.3×10^{-4}
Ne	I,II,III	5×10^{-5}
S	I,II,III,IV	9×10^{-6}

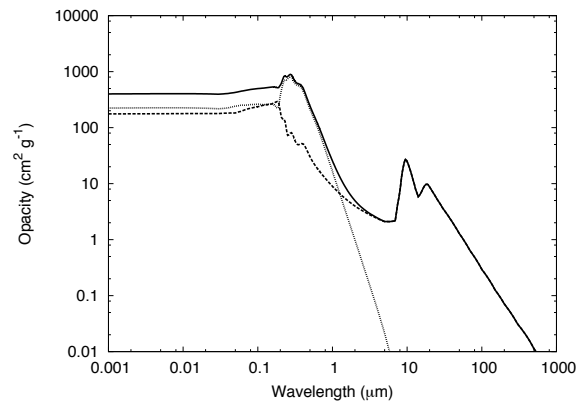


Figure 2. Total opacity (solid line), absorption opacity (dashed line) and scattering opacity (dotted line) per gramme of gas, plotted as a function of wavelength, for the $0.1 \mu\text{m}$ silicate dust grains used in the radiative transfer calculations.

no on-the-spot approximation). A total of 22 species are included in the photoionisation calculation, with abundances from Ferland (1995) as shown in Table 2. The star is represented by a blackbody source with a temperature of 40 000K and a luminosity of $L = 1.41 \times 10^6 L_\odot$ which produces an ionising photon flux of $7.45 \times 10^{49} \text{ s}^{-1}$.

The effects of dust opacity are included in the radiative transfer calculation, and separate gas and dust temperatures are calculated as the gas and dust are not expected to be thermally coupled. The dust grains are Draine and Lee silicates with a uniform size of $0.1 \mu\text{m}$ and a density of 3.6 g cm^{-3} . The total opacity (solid line), absorption opacity (dashed line) and scattering opacity (dotted line) per gramme of gas are plotted as a function of wavelength in Fig. 2 for the assumed dust to gas mass ratio of 0.01. A prescribed dust distribution is added to the hydrodynamics results (which do not include dust) as a post-processing step. The dust distribution is shown in Fig. 1 (top right). The free-flowing stellar wind (defined as any cell with a velocity greater than 1800 km s^{-1}) and the shocked wind (defined as any cell with a temperature greater than $1.1 \times 10^4 \text{ K}$) are dust free, and dust is present elsewhere.

There is substantial shock heating in the region between the forward shock and the stellar wind termination shock which is absent in a pure radiative transfer calculation. To account for this effect the temperature used by TORUS in

¹ www.astro.ex.ac.uk/people/th2/torus_html/homepage.html

² the number of cells in each dimension of the TORUS grid must be a power of 2 as TORUS uses a tree structure to store the grid

shocked stellar wind region (the region where the VH-1 temperature is greater than $1.1 \times 10^4 \text{K}$) is constrained to be at least as great as the temperature calculated by the VH-1 hydrodynamical calculation. The gas and dust temperatures calculated by TORUS are shown in the lower two panels of Fig. 1. The gas temperature in the inter-shock region is high ($\sim 10^7 \text{K}$) and in this part of the domain the temperature is governed by the results of the hydrodynamical calculation. In this inter-shock region the temperature will be determined by the balance between shock heating and radiative cooling, and both these processes are included in the VH-1 hydrodynamical calculation. Elsewhere the gas temperature is determined by the radiative transfer calculation and the lower temperatures (approximately 7000-9000K) are close to the corresponding temperature assumed in the hydrodynamical calculation (10^4K). All the gas in the simulation domain is highly ionised, consistent with the assumption of fully ionised gas in the hydrodynamical calculation. The dust temperature is much lower than the gas temperature and a “sunburst” pattern is seen in the dust temperature where dense knots in forward shock shadow the upstream dust. Similar features were seen in the planetary nebula simulations of Toalá & Arthur (2014).

4 SYNTHETIC OBSERVATIONS

The results from the photoionisation calculation were used to generate synthetic observations (infrared, $H\alpha$ and radio images and infrared SEDs). The temperature, density, abundance and dust distributions at the end of the photoionisation calculation are used to populate the TORUS grid with emissivities at the appropriate wavelength. A Monte-Carlo sampling technique (Harries 2000) is then used to sample the emission with a number of photon packets which are propagated through the grid (accounting for scattering and absorption events) to determine the flux in a prescribed image plane. The method has previously been applied to output from TORUS photoionisation calculations by Haworth et al. (2012).

4.1 Infrared images and SEDs

For generating infrared images and SEDs the emissivity of a grid cell ϵ_λ at a wavelength λ is given by

$$\epsilon_\lambda = B_\lambda(T) \kappa_\lambda \rho_{\text{ISM}} \quad (3)$$

where $B_\lambda(T)$ is the Planck function at temperature T , κ_λ is the wavelength dependent absorption opacity from dust, and ρ_{ISM} is the ISM gas density. Referring to Fig. 1 we see that the emissivity will be zero in the stellar wind (both shocked and un-shocked regions), as there is no dust and hence $\kappa_\lambda = 0$. The highest emissivities will be in the high density parts of the forward shock where the density and temperature (hence $B_\lambda(T)$) are high.

4.1.1 Images

Synthetic images at 22 microns and 12 microns are shown in the first and second rows of Fig. 3 respectively. The size of the images corresponds to 2.25 arcmin at a distance of 1 kpc and the colour scale is in distance independent units

of MJy sr^{-1} . To represent the effect of spatial resolution the 22 micron images have been smoothed with a 12 arcsec Gaussian filter and the 12 micron images have been smoothed with a 6.5 arcsec Gaussian filter. These resolutions have been chosen to match the resolution of WISE at these wavelengths. The pixel size of 2.75 arcsec was also chosen to match the properties of WISE. Images were also generated at 4.6 and 3.4 microns, but did not produce significant emission from the bow shock. We note that Povich et al. (2008) find their observed bow shocks are faint in the 3.4 micron IRAC band, consistent with our lack of emission at this wavelength.

At 0 degree inclination (not shown) the shock is viewed face-on and the emission is symmetric about the position of the star at the centre of the image. As we are viewing a 2D model along the axis of symmetry this is exactly as expected. At 30 degree inclination there is a noticeable asymmetry to the emission, with a peak ahead of the star. Although the morphology is not that of a classic bow shock there is still a clear infra-red excess ahead of the star. At 60 and 90 degree inclinations a more clearly identifiable bow shock morphology is seen, with a bright crescent of emission ahead of the star. Higher inclination angles have higher peak emission due to increased limb brightening of the shock cone (see Mac Low et al. (1991) for further discussion of the effects of viewing angle). The bow shock morphology is more clearly seen at 12 microns than at 22 microns as the spatial resolution is higher (6.5 arcsec compared to 12 arcsec). Infra-red observations of bow shocks show a crescent-shaped structure ahead of the star frequently with a bright spot near the apex (Kobulnicky et al. 2010; Peri et al. 2012). These structures are similar to our synthetic observations at 60 degree and 90 degree inclinations.

4.1.2 SEDs

Spectral energy distributions, as seen at 0 degree inclination (face-on; solid line) and 90 degree inclination (side on; dashed line) are shown in Fig. 4. The assumed distance is again 1 kpc. The top figure plots the SEDs as λF_λ and shows that at wavelengths shorter than $5 \mu\text{m}$ the emission is dominated by the star, and at wavelengths longer than $5 \mu\text{m}$ emission from hot dust in the bow shock dominates. This is consistent with the infrared images which show bow shock emission at 12 and $22 \mu\text{m}$, but not at 3.4 or $4.6 \mu\text{m}$. At 90 degree inclination the star is unobscured by bow shock material and the SED is similar to that of a star with an accretion disc viewed face-on (the optical depth along the path from the star to the observer is 0.427 at $0.1 \mu\text{m}$). At 0 degree inclination bow shock material obscures the star and the SED appears more like an SED from a star-disc system where the disc partially blocks direct stellar radiation (the optical depth along the path from the star to the observer is 2.57 at $0.1 \mu\text{m}$). The total luminosity of the SED is $1.22 \times 10^6 L_\odot$, compared to the stellar luminosity of $L = 1.41 \times 10^6 L_\odot$.

The lower figure plots the SEDs in mJy over the range $1\text{--}100 \mu\text{m}$ and solid points are from Candidate 7 of the Kobulnicky et al. (2010) sample, where circles are detections and triangles are upper limits. Candidate 7 is the most massive and energetic star in their sample and consequently is the best comparison to our model. In Fig. 4.1.2 the assumed

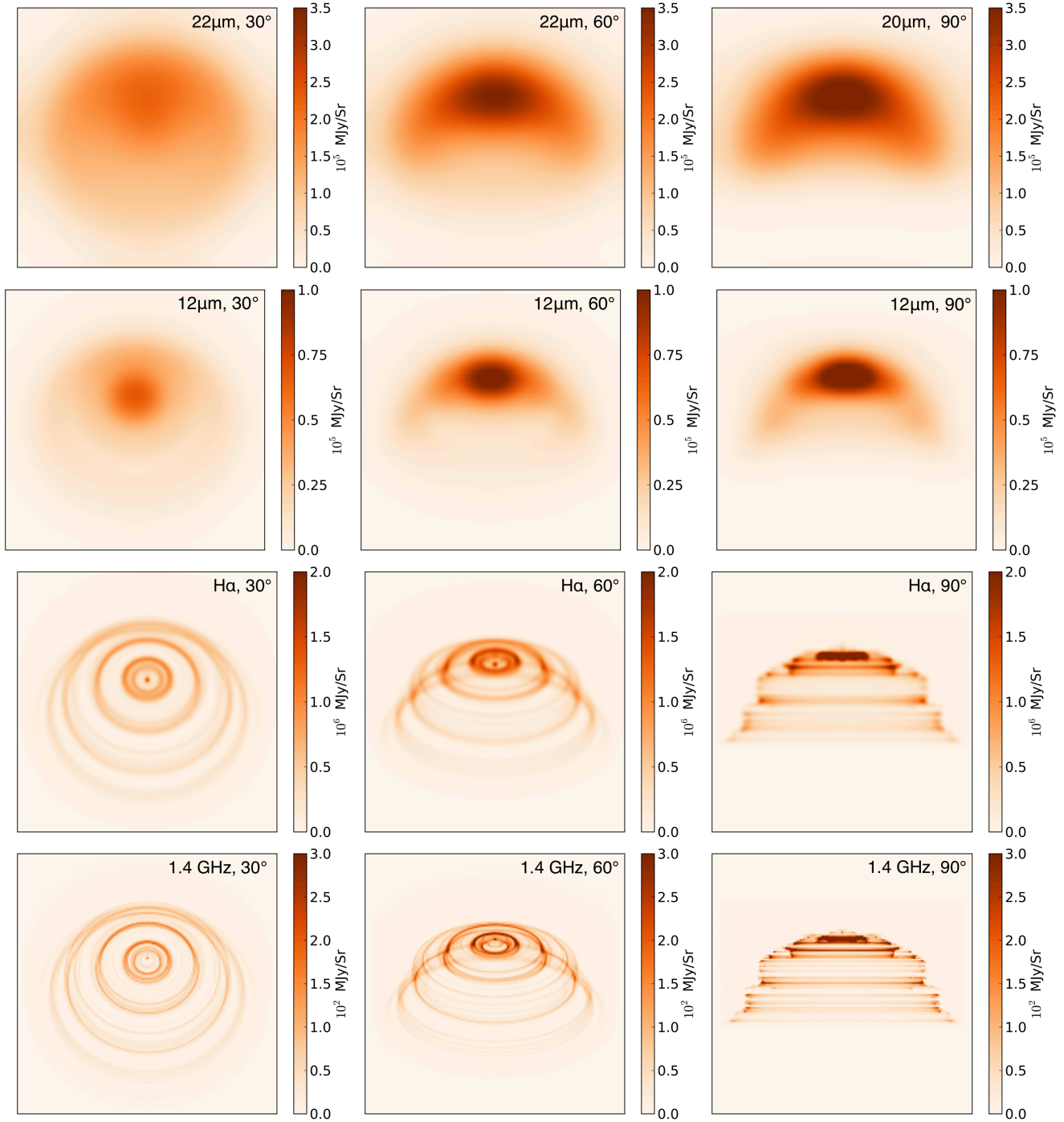


Figure 3. Synthetic images derived from the bow shock simulation. The top row and second row show infra-red images at $22\mu\text{m}$ (resolution = $12''$) and $12\mu\text{m}$ (resolution = $6.5''$) respectively. Third and fourth rows show $\text{H}\alpha$ (resolution = $1''$) and 1.4 GHz radio emission (no smoothing) respectively. Three inclination angles are shown: 30 degrees (left), 60 degrees (centre), 90 degree (right), where an inclination of zero corresponds to a line-of-sight which is parallel to the direction of motion of the star. The colour scale shows surface brightness in distance independent units of MJy sr^{-1} . The size of the images corresponds to 2.25 arcmin at a distance of 1 kpc, and the spatial resolution is stated in the individual figure captions.

distance is changed to 2.1 kpc to match the distance to candidate 7 in the Kobulnicky et al. (2010) sample. Kobulnicky et al. (2010) find their SED is consistent with a temperature of 40 000K for the star and Hanson (2003) finds an effective temperature of 46 131.8K and a luminosity $\log(L/L_{\odot}) = 5.51$ for the same star. By comparison

our model star has an effective temperature of 40 000K and $\log(L/L_{\odot}) = 6.15$, so is about 4.4 times more luminous but

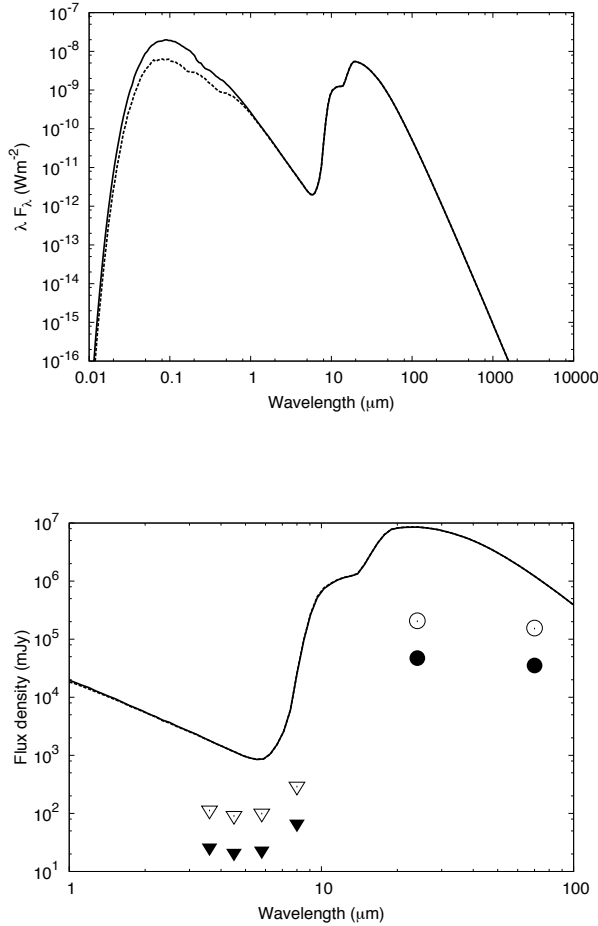


Figure 4. Spectral energy distributions from the star and bow shock viewed at 0 degree inclination (face on; dashed line) and 90 degree inclination (side on; solid line). Top: SED in SI units plotted as λF_λ vs wavelength in microns, bottom: SED in mJy vs wavelength in microns. At wavelengths shorter than $5 \mu\text{m}$ the emission is dominated by the star and at wavelengths longer than $5 \mu\text{m}$ emission from hot dust in the bow shock dominates. Solid circles are photometric points from Kobulnicky et al (2010) and solid triangles show upper limits. Open circles and open triangles show the Kobulnicky et al points scaled by a factor of 4.4 to account for our more luminous star.

with a similar temperature³. Open circles and open triangles show the Kobulnicky et al. (2010) Candidate 7 points scaled by a factor of 4.4 to account for our more luminous star. Compared to the observed photometric data points we have higher levels of emission, more than the factor of 4.4 in the stellar luminosity, although we have not included extinction effects in our model SED. The peak in the SED due to the bow shock appears at shorter wavelengths in our model SED than in the SED fitted to Candidate 7 by Kobulnicky et al. (2010). However the model has a smaller shock stand-off distance ($\sim 0.1\text{pc}$ for the model compared to a projected

distance of 0.53 pc for candidate 7) so it is reasonable to expect higher temperature material in the model bow shock (hence a shorter wavelength peak in the SED) and for more stellar radiation to be reprocessed through the bow shock (hence higher levels of emission). Meyer et al. (2014b) find that the bow shock luminosity scales strongly with stand-off distance in their models (stronger than R_0^3 according to their fig. 24). Such a strong dependence on R_0 indicates that a quantitative comparison between observed and model SEDs requires tuning the model parameters to produce a similar shock stand off distance to the observed object, as well as the inclusion of extinction.

4.2 H α images

When calculating H α images the emissivity of a grid cell is the sum of the recombination line emissivity and the dust emissivity (the latter is described in Section 4.1). For this model the dust emissivity from the bow shock is negligible in comparison to the recombination emissivity (the emission at $0.66\mu\text{m}$ seen in the SED shown in Fig. 4 is from the star and not the dust). However scattering from dust is significant at this wavelength (see Fig. 2), affecting emission in bright regions of the synthetic image by several per cent, so dust opacity is included in the calculations.

The H α line intensities are calculated using values from Hummer & Storey (1987), scaled according to the temperature dependence of the recombination coefficient in Table 1 of Storey & Hummer (1995). The Hummer & Storey (1987) line intensities are calculated relative to the H β line intensity given by

$$\epsilon_{H\beta} = 1.235 \times 10^{-25} n_e n_{H^+} \left(\frac{T}{10^4 \text{K}} \right)^{-0.87} \quad (4)$$

where the constant term is the emission measure given in Hummer & Storey (1987). The fiducial values are the case B values from Hummer & Storey (1987) for a density of $n = 10^2 \text{ cm}^{-3}$ and a temperature of 10^4 K .

All the gas in our model is highly ionised so the H α emissivity is effectively a function of temperature (to the power -0.87) and density squared. The emissivity of the stellar wind region is low due to the low density and high temperature. H α emission is expected to originate predominantly from the dense material at the forward shock. This region is bright in both infra-red emission and H α emission as it is dense, ionised, and contains dust.

H α images are shown in the third row of Fig. 3. The images have been blurred with a 1 arcsec Gaussian filter, representative of a high spatial resolution H α survey (e.g. IPHASS). The elliptical bands of emission seen at 30 and 60 degree inclinations, and the stripes seen at 90 inclination, are due to viewing a 2D simulation rotated about the axis of symmetry. The same effect was seen in the synthetic images of Raga et al. (1997) shown in their figure 5. In reality, and in a 3D simulation, we would expect these features to show bright knots of emission associated with instabilities at the forward shock (see Fig. 1).

The bow shock is more clearly identifiable in the H α images, with a more prominent bow morphology, due to the higher spatial resolution. If the H α images are smoothed to the same resolution as the infra-red images then the bow shock morphology is very similar. This is unsurprising given

³ The higher luminosity of our model star is required in order to be consistent with the stellar wind parameters used in Section 2

that the infra-red and H α emission both originate from the same region.

4.3 Radio images

When generating radio images we calculate thermal free-free emission from ionised hydrogen and the emissivity of a grid cell is given by

$$\epsilon_\nu = n_e^2 \alpha_{kk}(\nu, T) \exp\left(\frac{-h\nu}{kT}\right) \frac{2h\nu^3}{c^2} \quad (5)$$

where $\alpha_{kk}(\nu, T)$ is the free-free absorption coefficient for hydrogen at a frequency ν in a cell with temperature T (Mihalas & Mihalas 1984) and n_e^2 is the electron density. The dependance of the emissivity on the square of the electron density means that dense, ionised material within the forward shock again dominates the emission.

Synthetic radio observations at 1.4GHz are shown in the fourth row of Fig. 3. These images have not been spatially smoothed and hence show the sharpest features. Bands of emission associated with the 2D geometry are again seen, which in reality would correspond to knots of emission at the forward shock.

4.4 Emission slices and shock stand-off distance

Slices of intensity are shown in Fig 5 for 12 μ m (solid line), 22 μ m (dashed line) and H α (dotted line) for 30, 60 and 90 degree inclinations. For each slice the intensity has been normalised, by dividing by the maximum intensity, to enable the shape of the profiles to be more easily compared. The standoff distance R_0 , projected by the inclination angle, is shown as a solid vertical line. The x-axis is shown in parsecs and also arcseconds at a distance of 1 kpc.

At 90 degree inclination the peak of the 22 μ m emission is very close to the calculated stand-off distance of 0.1 pc. For the 12 μ m and H α emission the peaks are at a slightly greater distance but are also very close to 0.1 pc. The peaks of emission are closer to the calculated stand-off distance than might be expected given the position of the Wilkin analytical solution relative to the forward shock (see Fig. 1). At 60 degree inclination the infra-red peaks are in approximately the same location as at 90 degree inclination but the H α slice no longer shows a clear maximum. At 30 degree inclination the infra-red peaks are clearly separated with the 12 μ m peak closer to the star. Figure 6 again shows the 12 μ m (solid line) and 22 μ m (dashed line) intensity slices (previously plotted in the top left panel of Fig. 5) but also shows a 22 μ m slice smoothed to the same resolution as the 12 μ m slice (dotted line). This shows that the differences in the 12 μ m and 22 μ m profiles are not just due to resolution. The z-axis temperature profile in the region ahead of the star is shown in the bottom right panel of Fig. 5 (the star is at $z = 0$). A temperature gradient is seen with temperature decreasing in the upstream direction, consistent with the 12 μ m emission peaking closer to the star than the 22 μ m emission.

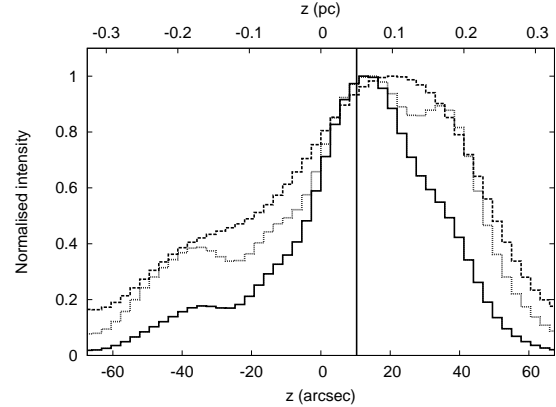


Figure 6. Intensity slices along the z-axis at 12 μ m (solid line) and 22 μ m (dashed line) for a 30 degree inclination angle. The dotted line is the intensity slice from the 22 μ m synthetic image smoothed to the same resolution as the 12 μ m synthetic image (i.e. 6.5 arcsec) to show resolution effects. The standoff distance R_0 , projected by the inclination angle, is shown as a solid vertical line.

5 DISCUSSION

5.1 Comparison with previous synthetic observations

Synthetic H α and dust continuum maps of a runaway star have been previously published by Raga et al. (1997), also using 2D hydrodynamical and radiative transfer calculations. Compared to our simulations Raga et al. (1997) have a much lower ISM density (1 cm^{-3} compared to 1000 cm^{-3}). In reality the ISM is far from homogeneous and a runaway star will encounter a range of ISM properties along its trajectory, hence both these regimes are of interest. Raga et al. (1997) also see the highest H α emissivity from the forward shock (see their fig. 4), and their H α and dust continuum maps (see their fig. 5) show significant similarities (although they note that the dust continuum has more extended emission in the bow shock wings).

Synthetic radio images were presented by Mac Low et al. (1991) and compared to observations of ultra-compact HII regions. In their model the emission emanates from a limb-brightened ionised shell, giving a similar morphology to our synthetic radio images. However their model does not form dense knots of material (the result of instabilities in the forward shock/contact discontinuity region) which give rise to the smaller scale structures seen in our synthetic observations.

More recently Meyer et al. (2014b), in their models of main sequence stars, find that “most of the emission by radiative cooling comes from shocked ISM gas which cools as the gas is advected from the forward shock to the contact discontinuity”. In our model the contact discontinuity and forward shock are not separated so there will not be advection from the forward shock to the contact discontinuity. However in both our model and the models of Meyer et al. (2014b) most infra-red emission is from dense regions associated with the forward shock.

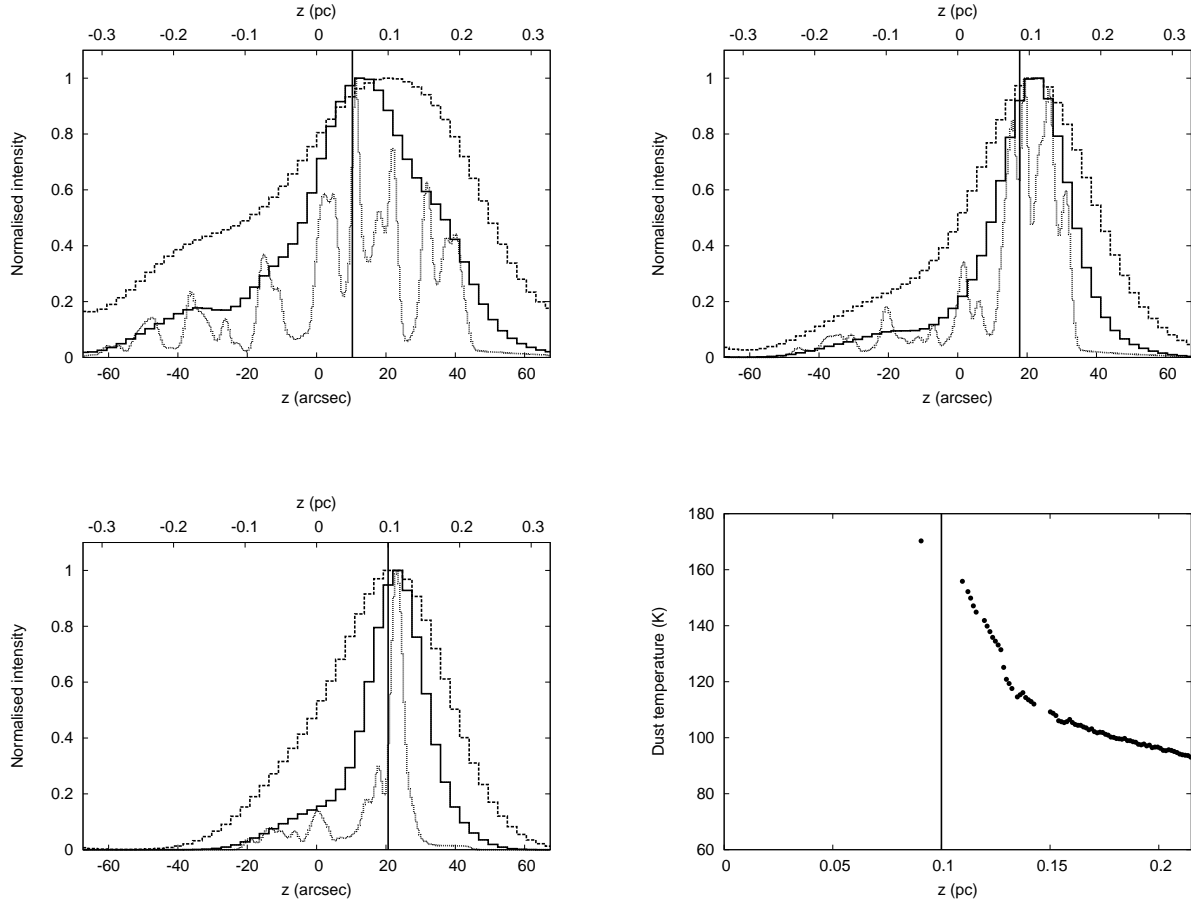


Figure 5. The first three panels show intensity slices along the z -axis at $12\mu\text{m}$ (solid line), $22\mu\text{m}$ (dashed line) and $\text{H}\alpha$ (dotted line), for inclinations of 30 (top left), 60 (top right) and 90 (bottom left) degrees. For each slice the intensity has been normalised by dividing by the maximum intensity. The standoff distance R_0 , projected by the inclination angle, is shown as a solid vertical line. The bottom right panel shows the dust temperature along the z -axis. The assumed distance is 1 kpc and the star located is at $z=0$.

5.2 Future model developments

Although our synthetic observations show an encouraging similarity in morphology to observations, and are consistent with previous synthetic observations, there are aspects of the model which will require further development if all relevant physical processes are to be taken into account.

The location and composition of the dust are subject to significant uncertainties but could have a significant influence on observables in the infra-red regime. Dust does not necessarily follow the gas distribution in a stellar bow shock (van Marle et al. 2011) with larger dust grains penetrating into the un-shocked stellar wind, and even the smaller grains can reach the wind termination shock (van Marle et al. 2015). Variations in dust composition, and presence of PAHs, can have a significant impact on infra-red observables (Kobulnicky et al. 2010; Pavlyuchenkov et al. 2013). Variations in composition can be driven by a number of mechanisms in addition to the effects described by van Marle et al. (2015) e.g. differing destruction time scales and the effects of radiation pressure (Ochsendorf et al. 2014).

Although our model provides a thorough treatment of

radiative transfer in the gas and dust, and accounts for the effects of shock heating, it does not self-consistently couple the hydrodynamics and radiative transfer. It is considerably more computationally expensive to run such a coupled calculation using Monte-Carlo radiative transfer, however such calculations have already been shown to be tractable in 3D using the TORUS code (Haworth & Harries 2012). Our current hydrodynamical model also does not include magnetic fields. van Marle et al. (2014) examine the effects of magnetic fields on the bow shock around an AGB star. They conclude that the main effect is suppression of instabilities, rather than an influence on the larger scale morphology. As our model involves significantly higher speeds for both the star and the stellar wind we will have a much higher ram pressure from both these components. Consequently the influence of the ISM magnetic field on the large scale structure will be even smaller than that seen by van Marle et al. (2014). However if magnetic fields are effective at suppressing instabilities this will affect the formation of the dense knots of material seen in our model, which are associated with prominent observable features.

6 CONCLUSIONS

We have generated synthetic images in infrared, H α and radio regimes for a runaway O star passing through a high density ISM. In all cases the emission is dominated by knots of dense material formed by instabilities at the forward shock. This region contains dust but is also ionised so it is seen not only at infra-red wavelengths (due to emission from warm dust) but is also seen in the H α recombination line and free-free radio emission. Differences in bow shock morphology are largely due to differing spatial resolution and the fundamental morphology is very similar (particularly as we have assumed that the dust distribution follows the gas distribution outside the stellar wind).

Synthetic infra-red SEDs show a similar shape to observed bow shock SEDs (Kobulnicky et al. 2010) but with higher levels of emission. This can be attributed partly to our model star being brighter than the observed stars but also to a smaller shock stand off distance. Achieving a better quantitative match to specific observations would require selecting model parameters which better represent the target of the observation. Variations in dust properties and the presence of PAHs may also need to be taken into account in order to achieve a quantitative match with observations.

ACKNOWLEDGMENTS

We would like to thank Pierre Lesaffre for a helpful review which significantly improved the paper. The TORUS calculations for this paper were performed on the DiRAC Complexity machine, jointly funded by STFC and the Large Facilities Capital Fund of BIS, and the University of Exeter Supercomputer, a DiRAC Facility jointly funded by STFC, the Large Facilities Capital Fund of BIS, and the University of Exeter.

REFERENCES

- Arnal E. M., Cichowolski S., Pineault S., Testori J. C., Cappa C. E., 2011, *A&A*, 532, A9
- Baranov V. B., Krasnobaev K. V., Ruderman M. S., 1976, *Ap&SS*, 41, 481
- Benaglia P., Romero G. E., Martí J., Peri C. S., Araudo A. T., 2010, *A&A*, 517, L10
- Blaauw A., 1961, *Bull. Astron. Inst. Netherlands*, 15, 265
- Blondin J. M., Mezzacappa A., DeMarino C., 2003, *ApJ*, 584, 971
- Bonnell I. A., Bate M. R., Clarke C. J., Pringle J. E., 1997, *MNRAS*, 285, 201
- Bonnell I. A., Vine S. G., Bate M. R., 2004, *MNRAS*, 349, 735
- Bressert E. et al., 2012, *A&A*, 542, A49
- Brown D., Bomans D. J., 2005, *A&A*, 439, 183
- Brown W. R., Cohen J. G., Geller M. J., Kenyon S. J., 2012, *ApJL*, 754, L2
- Colella P., Woodward P. R., 1984, *J. Comp. Phys.*, 54, 174
- Cameron F., Kaper L., 1998, *A&A*, 338, 273
- Cox N. L. J. et al., 2012, *A&A*, 537, A35
- Cruz-González C., Recillas-Cruz E., Costero R., Peimbert M., Torres-Peimbert S., 1974, *RevMexAA*, 1, 211
- de Wit W. J., Testi L., Palla F., Zinnecker H., 2005, *A&A*, 437, 247
- Dgani R., van Buren D., Noriega-Crespo A., 1996, *ApJ*, 461, 372
- Ercolano B., Barlow M. J., Storey P. J., Liu X.-W., 2003, *MNRAS*, 340, 1136
- Ferland G., 1995, in *The Analysis of Emission Lines: A Meeting in Honor of the 70th Birthdays of D. E. Osterbrock & M. J. Seaton*, R. Williams & M. Livio, ed., p. 83
- Gáspár A., Su K. Y. L., Rieke G. H., Balog Z., Kamp I., Martínez-Galarza J. R., Stapelfeldt K., 2008, *ApJ*, 672, 974
- Gratier P., Pety J., Boissé P., Cabrit S., Lesaffre P., Gerin M., Pineau des Forêts G., 2014, *A&A*, 570, A71
- Gvaramadze V. V., Menten K. M., Kniazev A. Y., Langer N., Mackey J., Kraus A., Meyer D. M.-A., Kamiński T., 2014, *MNRAS*, 437, 843
- Hanson M. M., 2003, *ApJ*, 597, 957
- Harries T. J., 2000, *MNRAS*, 315, 722
- Hawley J., Blondin J., Lindahl G., Lufkin E., 2012, *VH-1: Multidimensional ideal compressible hydrodynamics code*. Astrophysics Source Code Library
- Haworth T. J., Harries T. J., 2012, *MNRAS*, 420, 562
- Haworth T. J., Harries T. J., Acreman D. M., 2012, *MNRAS*, 426, 203
- Haworth T. J., Harries T. J., Acreman D. M., Bisbas T. G., 2015, *MNRAS*, 453, 2277
- Hills J. G., 1988, *Nature*, 331, 687
- Hoogerwerf R., de Bruijne J. H. J., de Zeeuw P. T., 2000, *ApJL*, 544, L133
- Hoogerwerf R., de Bruijne J. H. J., de Zeeuw P. T., 2001, *A&A*, 365, 49
- Hummer D. G., Storey P. J., 1987, *MNRAS*, 224, 801
- Huthoff F., Kaper L., 2002, *A&A*, 383, 999
- Kobulnicky H. A., Gilbert I. J., Kiminki D. C., 2010, *ApJ*, 710, 549
- Krumholz M. R., Klein R. I., McKee C. F., Offner S. S. R., Cunningham A. J., 2009, *Science*, 323, 754
- Larson R. B., 1992, *MNRAS*, 256, 641
- Leonard P. J. T., 1991, *AJ*, 101, 562
- López-Santiago J. et al., 2012, *ApJL*, 757, L6
- Mac Low M.-M., van Buren D., Wood D. O. S., Churchwell E., 1991, *ApJ*, 369, 395
- Mackey J., Mohamed S., Neilson H. R., Langer N., Meyer D. M.-A., 2012, *ApJL*, 751, L10
- Meyer D. M.-A., Gvaramadze V. V., Langer N., Mackey J., Boumis P., Mohamed S., 2014a, *MNRAS*, 439, L41
- Meyer D. M.-A., Mackey J., Langer N., Gvaramadze V. V., Mignone A., Izzard R. G., Kaper L., 2014b, *MNRAS*, 444, 2754
- Mihalas D., Mihalas B. W., 1984, *Foundations of radiation hydrodynamics*. Oxford University Press
- Noriega-Crespo A., van Buren D., Cao Y., Dgani R., 1997a, *AJ*, 114, 837
- Noriega-Crespo A., van Buren D., Dgani R., 1997b, *AJ*, 113, 780
- Ochsendorf B. B., Cox N. L. J., Krijt S., Salgado F., Berné O., Bernard J. P., Kaper L., Tielens A. G. G. M., 2014, *A&A*, 563, A65
- Pavlyuchenkov Y. N., Kirsanova M. S., Wiebe D. S., 2013, *Astronomy Reports*, 57, 573
- Peri C. S., Benaglia P., Brookes D. P., Stevens I. R., Ise-

- quilla N. L., 2012, *A&A*, 538, A108
- Portegies Zwart S. F., 2000, *ApJ*, 544, 437
- Poveda A., Ruiz J., Allen C., 1967, *Boletín de los Observatorios Tonantzintla y Tacubaya*, 4, 86
- Povich M. S., Benjamin R. A., Whitney B. A., Babler B. L., Indebetouw R., Meade M. R., Churchwell E., 2008, *ApJ*, 689, 242
- Raga A. C., Noriega-Crespo A., Cantó J., Steffen W., van Buren D., Mellema G., Lundqvist P., 1997, *RevMexAA*, 33, 73
- Schure K. M., Kosenko D., Kaastra J. S., Keppens R., Vink J., 2009, *A&A*, 508, 751
- Storey P. J., Hummer D. G., 1995, *MNRAS*, 272, 41
- Tetzlaff N., Neuhauser R., Hohle M. M., 2011, *MNRAS*, 410, 190
- Toalá J. A., Arthur S. J., 2014, *MNRAS*, 443, 3486
- van Buren D., McCray R., 1988, *ApJL*, 329, L93
- van Marle A. J., Decin L., Cox N., Meliani Z., 2015, *J. Phys.: Conf. Ser.*, 577, 012024
- van Marle A. J., Decin L., Meliani Z., 2014, *A&A*, 561, A152
- van Marle A. J., Meliani Z., Keppens R., Decin L., 2011, *ApJL*, 734, L26
- Villaver E., Manchado A., García-Segura G., 2012, *ApJ*, 748, 94
- Vishniac E. T., 1994, *ApJ*, 428, 186
- Wilkin F. P., 1996, *ApJL*, 459, L31
- Wolfire M. G., Cassinelli J. P., 1987, *ApJ*, 319, 850
- Wood K., Mathis J. S., Ercolano B., 2004, *MNRAS*, 348, 1337
- Yorke H. W., Sonnhalter C., 2002, *ApJ*, 569, 846
- Zinnecker H., 1982, *Annals of the New York Academy of Sciences*, 395, 226